# Vortex statistics in turbulent rotating convection

R. P. J. Kunnen,[1,*] H. J. H. Clercx,[1,2,†] and B. J. Geurts[2,1,‡]

[1]*Fluid Dynamics Laboratory, Department of Physics, International Collaboration for Turbulence Research (ICTR) and J. M. Burgers Center for Fluid Dynamics, Eindhoven University of Technology, P.O. Box 513, 5600 MB Eindhoven, The Netherlands*

[2]*Department of Applied Mathematics and J. M. Burgers Center for Fluid Dynamics, University of Twente, P.O. Box 217, 7500 AE Enschede, The Netherlands*

(Received 26 February 2010; revised manuscript received 14 July 2010; published 8 September 2010)

The vortices emerging in rotating turbulent Rayleigh-Bénard convection in water at Rayleigh number Ra $=6.0\times10^8$ are investigated using stereoscopic particle image velocimetry and by direct numerical simulation. The so-called $Q$ criterion is used to detect the vortices from velocity fields. This criterion allows distinguishing vorticity- and strain-dominated regions in the flow by decomposing the velocity gradient tensor into symmetric and antisymmetric parts. Vortex densities, mean vortex radii and mean vortex circulations are calculated at two horizontal cross-sections of the cylindrical flow domain and at several rotation rates, described by the Taylor number which takes values between $3.0\times10^8$ and $7.7\times10^{10}$. Separate statistics are calculated for cyclonic and anticyclonic vortices. Vortex densities and mean vortex radii are mostly independent of the Taylor number except very close to the bottom and top plates where more vortices are detected when the Taylor number is raised (rotation increases). The vortex population close to the plate consists mostly of cyclones while further into the bulk of the domain a similar amount of cyclones and anticyclones is found. The cyclonic vortices contain more circulation than the anticyclones. The same vortex analysis of the simulation results at additional vertical positions revealed that the vortices are formed in a boundary layer on the plate with a thickness of approximately two Ekman lengths.

DOI: 10.1103/PhysRevE.82.036306 PACS number(s): 47.55.pb, 47.32.Ef, 47.27.De

## I. INTRODUCTION

Rotating Rayleigh-Bénard convection is relevant for many geophysical and astrophysical flow phenomena, as well as industrial processes. A remarkable feature of convective flows affected by rotation is the formation of vortical structures. Many examples are found in the geophysical and astrophysical context: Earth's atmosphere [1] and oceans [2], and the interior flows of the gaseous planets [3] and the Sun [4]. For example, oceanic deep convection occurs when, in winter, surface cooling in the Arctic and Antarctic seas may lead to long-lived vortical downward flow [2,5]. This deep ventilation is of paramount importance for the global thermohaline circulation. An example of an industrial process where similar vortices occur is chemical vapor deposition on a heated rotating deposition target [6]. The omnipresence of these vortices in nature and technology has prompted us to perform a closer investigation of vortices in turbulent rotating convective flows.

The canonical example of a rotating convective flow is the rotating Rayleigh-Bénard problem [7]: a fluid layer enclosed by horizontal plates is heated from below, cooled from above, and subjected to a vertically aligned rotation. This flow problem can be concisely described with three dimensionless parameters. The Rayleigh number Ra represents the strength of the temperature gradient, the Prandtl number $\sigma$ describes the diffusive properties of the fluid, and the Taylor number Ta is a dimensionless representation of the rotation rate:

$$\mathrm{Ra}\equiv\frac{g\alpha\Delta T H^3}{\nu\kappa},\quad \sigma\equiv\frac{\nu}{\kappa},\quad \mathrm{Ta}\equiv\left(\frac{2\Omega H^2}{\nu}\right)^2. \qquad (1)$$

Here $g$ is the gravitational acceleration, $H$ the height of the fluid layer, $\Delta T$ the temperature difference applied between bottom and top plates, $\Omega$ the rotation rate, and $\nu$, $\kappa$, and $\alpha$ are the kinematic viscosity, thermal diffusivity and thermal expansion coefficient of the fluid, respectively. In practical applications of Rayleigh-Bénard convection a lateral confinement must be introduced. A popular geometry for experiments is an upright cylinder. The extra parameter to describe the geometry is the diameter-to-height aspect ratio $\Gamma\equiv D/H$, with $D$ the diameter of the cylinder. We will also use the Ekman number $\mathrm{Ek}\equiv 2/\sqrt{\mathrm{Ta}}$. Another commonly used dimensionless number in this context is the Rossby number $\mathrm{Ro}\equiv\sqrt{\mathrm{Ra}/\sigma\mathrm{Ta}}$, which is the ratio of the rotational time scale $\tau_\Omega\equiv 1/2\Omega$ to the buoyant time scale $\tau_b\equiv\sqrt{H/g\alpha\Delta T}$.

It is well-known that vertically aligned columnar vortices are the dominant flow structures in rapidly rotating turbulent Rayleigh-Bénard convection [8–17]. These vortical plumes are the most active components in the flow, as almost all of the vertical transport of fluid and heat is found in the interior of these vortices. In spite of their relevance for the flow dynamics, only a few studies report on the statistics of these vortices. The major problem lies with the vortex identification, as it is not *a priori* clear what constitutes a vortex. Earlier works generally used flow visualizations of rotating Rayleigh-Bénard convection in which the vortices were identified by eye [8,9,13], thus introducing arbitrariness into the

*Present address: Institute of Aerodynamics, RWTH Aachen University, Wüllnerstrasse 5a, 52062 Aachen, Germany; r.kunnen@aia.rwth-aachen.de

†h.j.h.clercx@tue.nl

‡b.j.geurts@utwente.nl

 

TABLE I. Reported scalings of the vortex number density $N$ (number of vortices per area in a horizontal plane) with Ta. When available, the vortex number density is reported separately for cyclonic ($N_+$) and anticyclonic ($N_-$) vortices. In all of these studies the convecting fluid was water with Prandtl number close to 6. Boubnov and Golitsyn [8] used a convection cell without a top plate. Therefore, they cannot specify the Rayleigh number Ra, but instead use the flux Rayleigh number $\mathrm{Ra_f} \equiv \mathrm{RaNu}$. Sakai [9] presented a theory which actually predicts a smooth transition between the two limiting cases given here, accompanied by an experimental validation. For reference, we include approximate scaling exponents for the current results depicted in Fig. 5(b). These results match best with the top-view vortex detection used in the other works compiled in this Table.

| Author(s) | Ra | $N$ scaling | Range | Remarks |
|---|---|---|---|---|
| Boubnov and Golitsyn [8] | $\mathrm{Ra_f}=\mathrm{RaNu}=10^6-2\times10^{11}$ | $N\sim\mathrm{Ta}^{1/3}$ | $24.5<\mathrm{Ta}/\mathrm{Ra_f}<200$ $(10^6<\mathrm{Ta}<10^{12})$ | Steady hexagonal vortex grid, scaling from linear theory [7]. Experimental validation in open-topconvection cell with vortex counting from streak-line photography. |
| | | $N\sim\mathrm{Ta}^{1/2}$ | $0.003<\mathrm{Ta}/\mathrm{Ra_f}<24.5$ $(10^6<\mathrm{Ta}<10^{12})$ | Unsteady vortex grid. Experimentally obtained correlation. |
| Sakai [9] | $10^6-10^9$ | $N\sim\mathrm{Ta}^{-1/4}$ | $\mathrm{Ro}\uparrow 1$ | Limit of theory based on geostrophic equilibrium validated with vortex counting in large-$\Gamma$ convection cell with water containing thermochromic crystals for visualization. |
| | | $N\sim\mathrm{Ta}^{3/4}$ | $\mathrm{Ta}\uparrow\mathrm{Ta_c}$ | Limit of aforementioned theory for Ta approaching its critical value [7]. |
| Vorobieff and Ecke [10] | $2\times10^8$ | $N\sim\mathrm{Ta}^{1/2}$ | $6.4\times10^7\lesssim\mathrm{Ta}\lesssim2.6\times10^{10}$ | Vortices counted from visualizations using thermochromic crystals. |
| Vorobieff and Ecke [11] | $3.2\times10^8$ | $N_+\sim\mathrm{Ta}^{1/2}$ | $1.5\times10^7\lesssim\mathrm{Ta}\lesssim1\times10^{10}$ | PIV measurements; Eq. (5) is applied to detect vortical regions. Cyclonic and anticyclonic vortices counted separately. |
| | | $N_-\sim\mathrm{Ta}^{1/2}$ | $9\times10^8\lesssim\mathrm{Ta}\lesssim1\times10^{10}$ | |
| This work | $6\times10^8$ | $N_+\sim\mathrm{Ta}^{0.2}$ | $1.2\times10^9\lesssim\mathrm{Ta}\lesssim7.7\times10^{10}$ | DNS; Eq. (4) is used for vortex detection. |
| Figure 5(b) | | $N_-\sim\mathrm{Ta}^{0.3}$ | $4.8\times10^9\lesssim\mathrm{Ta}\lesssim7.7\times10^{10}$ | Reported power laws should be interpreted as indicative scalings for comparison with other works; no strong evidence of power-law scaling is found. |

results. More recently, digital particle image velocimetry (PIV) [18] has been applied by Vorobieff and Ecke [11,15]. The velocity field snapshots had adequate resolution for vortex detection based on a criterion utilizing the discrete derivatives of velocity. This criterion allows distinguishing vorticity- and strain-dominated regions in the flow by decomposing the velocity gradient tensor into symmetric and antisymmetric parts, where vorticity-dominated regions are identified as vortices. Mean vortex radii and vortex densities were reported. In another study by these authors [10] the vortices were visualized with thermochromic crystals. In Table I, we summarize the results concerning the dependence of the vortex number density $N$ on the rotation rate (Taylor number) reported in the aforementioned works. It must be noted that these studies (including this work) are in a parameter range which is far away from the true geo-/astrophysical flows.

The following papers also deal with the vortices in turbulent rotating convection, although they do not directly consider vortex number density. Descriptions of the vortices found in numerical simulations of turbulent rotating convection were given by Julien *et al.* [14]. In a subsequent investigation, Sprague *et al.* [16] presented detailed visualizations from their numerical simulation of the asymptotically reduced equations valid for strong rotation. In these numerical studies no vortex number or vortex size statistics were gathered. Portegies *et al.* [19] formulated a theoretical model for the vortices and compared the model vortex with an ensemble-averaged vortex from numerical simulation.

In the present investigation we gather vortex statistics from experiments employing stereoscopic PIV (SPIV) and from direct numerical simulation (DNS). From the velocity data the so-called $Q$ criterion [20,21] is calculated. Statistics of the mean amount of vortices in a horizontal cross-section and the mean radius and circulation per vortex are presented as a function of rotation rate, separately for cyclonic and anticyclonic vortices. This work is to our knowledge the first to consider vortex statistics in rotating convection with numerical simulations using the aforementioned criterion. The main advantage of DNS over PIV/SPIV is the availability of the full velocity gradient tensor, while with PIV/SPIV only in-plane velocity derivatives can be determined. Thus in the DNS we can apply the $Q$ criterion directly, precluding any assumptions on the vertical structure as required for SPIV. Still, there is a favorable agreement between DNS and SPIV. In addition, the use of several horizontal planes for vortex detection in the DNS provides insight into the vertical dependence of the vortex statistics, and thus into the typical vertical structure of the vortices.

We first describe the experimental and numerical methods used in this work in Sec. II. Then, the vortex detection pro-

cedure is elucidated in Sec. III, which also contains the presentation of the vortex statistics. Finally, we summarize our findings in Sec. IV.

## II. METHODS

The vortex state in turbulent rotating convection is studied with both numerical simulations and experiments employing SPIV. An overview of the numerical approach is given in Sec. II A. The experimental setup is the same as in our previous works [22–25]; we briefly repeat the most important parts in Sec. II B.

### A. Numerical arrangement

The equations to be solved are the incompressible Navier-Stokes and temperature equations including rotation with application of the Boussinesq approximation [7],

$$\frac{\partial \mathbf{u}}{\partial t} + (\mathbf{u}\cdot\boldsymbol{\nabla})\mathbf{u} + \sqrt{\frac{\sigma \mathrm{Ta}}{\mathrm{Ra}}}\hat{\mathbf{z}}\times\mathbf{u} = -\boldsymbol{\nabla}p + \sqrt{\frac{\sigma}{\mathrm{Ra}}}\nabla^2\mathbf{u} + T\hat{\mathbf{z}}, \tag{2a}$$

$$\frac{\partial T}{\partial t} + (\mathbf{u}\cdot\boldsymbol{\nabla})T = \frac{1}{\sqrt{\sigma \mathrm{Ra}}}\nabla^2 T, \tag{2b}$$

$$\boldsymbol{\nabla}\cdot\mathbf{u} = 0, \tag{2c}$$

with $\mathbf{u}$ the velocity vector, $p$ the reduced pressure (including the centrifugal acceleration potential), $T$ the temperature and $\hat{\mathbf{z}}$ the vertical unit vector pointing counter to gravity. These equations are made dimensionless with the scaling variables $H$ for length, $\Delta T$ for temperature and $\tau_\mathrm{b}$ for time. Velocity is thus scaled with the buoyant velocity $U \equiv H/\tau_\mathrm{b}$, which is also referred to as the free-fall velocity [26,27]. The equations, written in cylindrical coordinates $(r,\phi,z)$, are solved in a cylindrical volume of aspect ratio $\Gamma = 1$. No-slip velocity boundary conditions are applied on all walls. The sidewall is adiabatic: $\partial T/\partial r = 0$ at $r = H/2$. The top and bottom walls have constant temperatures: $T = 1$ at $z = 0$ (bottom wall) and $T = 0$ at $z = H$ (top wall).

The governing equations are discretized with second-order accurate finite- difference approximations. The equations of motion in cylindrical coordinates possess factors of $1/r$. By writing the equations in terms of the vector $(ru_r, u_\phi, u_z)$ and the use of a staggered grid these singularities are alleviated: only the radial velocity component needs to be evaluated at $r = 0$, where $ru_r = 0$. Time-integration is done with a third-order Runge-Kutta scheme. The spatial and temporal discretization is described in more detail in [27–29].

All simulations adopt $\mathrm{Ra} = 6.0 \times 10^8$ and $\sigma = 6.4$. Different Taylor numbers are used: $\mathrm{Ta} = 3.0 \times 10^8$, $1.2 \times 10^9$, $4.8 \times 10^9$, $1.9 \times 10^{10}$, and $7.7 \times 10^{10}$. The grid resolution is $n_r \times n_\phi \times n_z = 193 \times 385 \times 385$. The points in the azimuthal direction are distributed evenly. Close to the bottom and top walls, as well as close to the sidewall, there is a denser grid in order to resolve the boundary layers formed there. It has been validated [25] that this grid meets the resolution requirements even for the higher Rayleigh number $\mathrm{Ra} = 1.0 \times 10^9$.

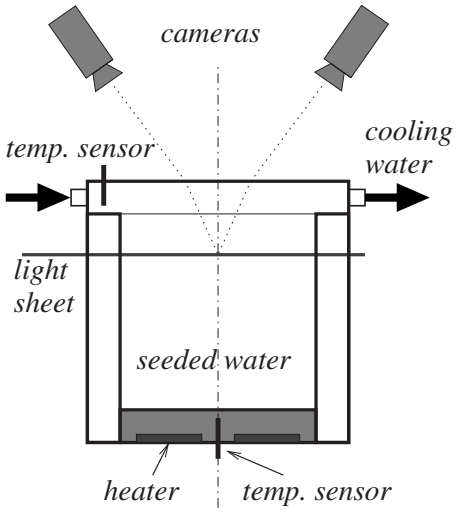


FIG. 1. Sketch of the experimental setup.

### B. Experimental arrangement

The convection cell is schematically depicted in Fig. 1. A cylinder of dimensions $H = D = 230$ mm filled with water is closed from below by a copper block with an electric heater underneath. At the top, cooling water is circulated through a transparent cooling chamber, separated from the working fluid by a thin (1 mm) Plexiglas sheet. Bottom and top temperatures are controlled with temperature sensors and controllers; the applied temperature difference is $\Delta T = 5$ K which would correspond to a Rayleigh number $\mathrm{Ra} = 1.11 \times 10^9$. However, due to the temperature drop over the Plexiglas plate the effective Rayleigh number is estimated to be $\mathrm{Ra}_\mathrm{eff} \approx 6 \times 10^8$ [25]. The mean operating temperature is 24 °C which corresponds to a Prandtl number $\sigma = 6.37$. The temperature at the top is constant up to $\pm 0.04$ K; at the bottom up to $\pm 0.02$ K. The water inside the cylinder is seeded with 50-$\mu$m-diameter polyamid seeding particles. The cylinder is enclosed in a square container, with the volume in between also filled with water. This allows the crossing of a horizontal laser light sheet at 45 mm from the top without too much refraction. Two cameras at different viewpoints record the particle images. A stereoscopic particle image velocimetry (SPIV) algorithm [30] processes the images into three-component two-dimensional velocity vector fields consisting of $53 \times 55$ vectors, with vector separations $\Delta x = 2.30$ mm and $\Delta y = 2.78$ mm, respectively. The rectangular measurement area thus covers roughly $120 \times 150$ mm$^2$, not the full circular cross-section of the cylinder. All equipment is placed on a rotating table. In this paper, we focus on the experiments in the rotation-dominated regime with Rossby numbers below one in order to arrive at the vortex-dominated flow regime. The Taylor number takes values $\mathrm{Ta} = 3.4 \times 10^8$, $1.4 \times 10^9$, $5.4 \times 10^9$, and $2.2 \times 10^{10}$. Using the current setup it was not possible to further raise the Taylor number. Fifteen velocity fields are measured per second,

with a duration of over 11 min (approximately $10^4$ fields) per experiment.

## III. VORTEX IDENTIFICATION

In this section we introduce in detail the vortex detection criteria used in DNS and SPIV, followed by an illustration of the three-dimensional structure of the vortices. Then the vortex statistics are presented, separated into an analysis at constant height (DNS and SPIV) and an analysis in which the heights are chosen based on the rotation-dependent Ekman layer thickness (DNS only).

### A. Preliminaries

It is not *a priori* clear what exactly constitutes a vortex. Vorticity is an obvious first-hand criterion, but vorticity is also found in shear-dominated flow regions. Therefore, more elaborate quantities need to be used. Many authors, e.g., Refs. [20,21,31–34], have provided criteria that can be used for the detection of vortices, mostly based on the velocity gradient tensor $\nabla \mathbf{u} = \partial_i u_j$ $(i,j \in \{1,2,3\})$. This tensor can be split into a symmetric and antisymmetric part,

$$\nabla \mathbf{u} = \frac{1}{2}[\nabla \mathbf{u} + (\nabla \mathbf{u})^T] + \frac{1}{2}[\nabla \mathbf{u} - (\nabla \mathbf{u})^T] = \mathrm{S} + \Omega, \qquad (3)$$

where S, the symmetric part, is also known as the rate-of-strain tensor, and $\Omega$, the antisymmetric part, is also known as the vorticity tensor (the superscript $^T$ indicates the matrix transpose).

A criterion introduced in [20], intended for three-dimensional flows, is the so-called $Q$ criterion. This criterion defines a vortex as a spatial region where

$$Q_{3D} \equiv \frac{1}{2}(\|\Omega\|^2 - \|\mathrm{S}\|^2) > 0, \qquad (4)$$

where $\|\mathrm{A}\| = \sqrt{\mathrm{Tr}(\mathrm{A}\mathrm{A}^T)}$ represents the Euclidean norm of the tensor A. An equivalent criterion for two-dimensional flows, now known as the Weiss function, was introduced independently by Obuko [31] and Weiss [33]. The usual definition of the Weiss function has a minus sign when compared to Eq. (4) and hence regions for which the Weiss function is negative are considered vortices.

Vorobieff and Ecke [11,15] used a criterion formulated for two-dimensional horizontal-velocity data perpendicular to $\hat{\mathbf{z}}$, based on the local flow topology as introduced in [32]: within vortices the eigenvalues of the two-dimensional variant $\nabla \mathbf{u}|_{2D} = \partial_i u_j$ $(i,j \in \{1,2\})$ are complex. The vortex detection criterion is then Eq. (2) in [15]; here we add a minus sign for compliance with the three-dimensional definition:

$$Q_{2D} \equiv 4\ \mathrm{Det}(\nabla \mathbf{u}|_{2D}) - [\mathrm{Tr}(\nabla \mathbf{u}|_{2D})]^2 > 0. \qquad (5)$$

We remark that the two-dimensional form of Eq. (4), the Weiss function [31,33], is identical to Eq. (5), which is again identical to the formulation used by Vorobieff and Ecke [11,15] apart from the sign.

In practice the threshold value zero to discern vortices from the surrounding flow was found to be unsuitable. The discrete representation of the velocity field introduces discretization errors that add small fluctuations to the calculated $Q$ values. Contours at $Q=0$ had therefore highly irregular shapes. We apply a somewhat higher positive threshold value in the vortex detection, which produces smoother and more convex contours that are more in line with the vortex shape as inferred from velocity field snapshots.

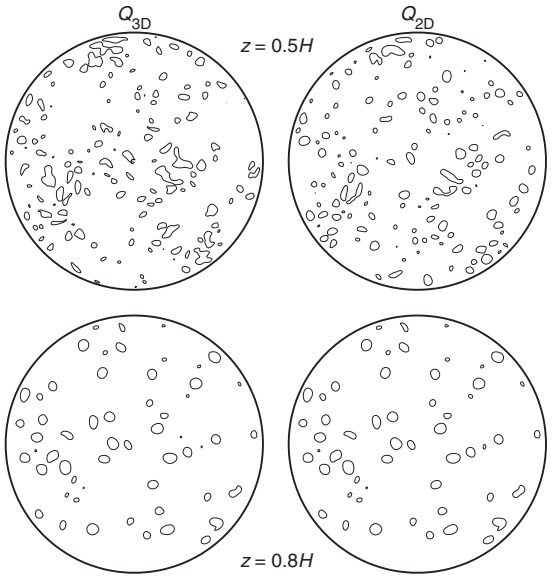


FIG. 2. A comparison between the three-dimensional criterion $Q_{3D}$ and the two-dimensional criterion $Q_{2D}$ for vortex identification. Contours indicating the circumference of vortical regions are shown in horizontal cross sections of the cylinder at $z=0.5H$ (upper row) and at $z=0.8H$ (lower row), for a simulation at $\mathrm{Ta}=7.7\times10^{10}$.

The simulations provide the opportunity to compare the two-dimensional criterion $Q_{2D}$ with the full three-dimensional $Q_{3D}$ criterion. In Fig. 2, for a rotation-dominated case at $\mathrm{Ta}=7.7\times10^{10}$, contours based on these criteria plotted at $z=0.5H$ and at $z=0.8H$ are compared. It can be concluded that the two criteria are nearly interchangeable at $z=0.8H$. This correspondence has also been validated for other rotation rates. It can thus be anticipated that the use of $Q_{2D}$ in the experimental data does not lead to different conclusions when compared with the numerical results for which the full three-dimensional $Q_{3D}$ criterion can be applied. At $z=0.5H$, however, there are considerable differences. In order to detect vortices at that height the full three-dimensional criterion must be applied, which is not accessible with the current measurement technique. It is also found that at $z=0.5H$ the shapes of the vortical regions are no longer (near-) ellipsoids due to mutual vortex interactions such as merger [14].

Vorobieff and Ecke [11,15] also employed instantaneous streamlines to get an impression of the distribution of the out-of-plane vertical velocity, which is inaccessible with regular one-camera PIV. In Appendix, this approach is tested using the current experimental and numerical results, including measurements of the vertical velocity. It is found that the resolution greatly influences the streamline trajectories; unphysical and arbitrary results are found concerning the

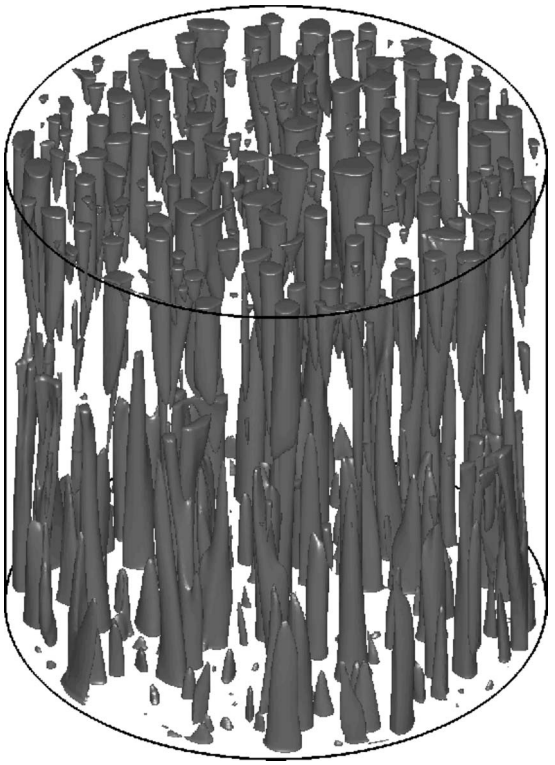

FIG. 3. Snapshot of $Q_{3D}$ isosurfaces at $\mathrm{Ta}=7.7\times10^{10}$.

apparent distribution of vertical velocity. Therefore we do not include instantaneous streamlines in the current analysis.

### B. Spatial structure

The $Q_{3D}$ criterion applied on the entire computational domain in the numerical simulation gives an indication of the spatial structure of vortices inside the domain. Such a snapshot is presented in Fig. 3 at $\mathrm{Ta}=7.7\times10^{10}$. The threshold value that is used to make this isosurface plot is $Q=0.97$, which is one hundredth of the maximal $Q$ found in this snapshot. A threshold slightly above zero avoids the inclusion of small- scale fluctuations arising in the numerical derivatives visible at relatively quiescent regions. From the isosurface plot it can be appreciated that the vortices are largest and most numerous near the top and bottom plates. Also, most vortices do not stretch from top to bottom: the vortices, on entering the bulk, gradually lose vorticity, and experience spin-down when approaching the opposite plate. Such an arrangement is readily observed in the visualizations of [9]. The vortices are weakest around the midplane $z=0.5H$; at this height it is therefore hardest to discern the vortices from the inherent background fluctuations.

A comparison of snapshots of $Q_{3D}$ at other Ta is presented in Fig. 4. The $Q_{3D}$ value for the isosurface is again one hundredth of the maximal $Q_{3D}$ found in the snapshot. At lower rotation rates (lower Ta, higher Ro) considerably increased vertical variations are found. The columnar flow as expected from the Taylor-Proudman theorem is only found at the highest Ta. At the lower Ta values an intricate network of entangled vortical tubes is found in the central part of the cylinder.

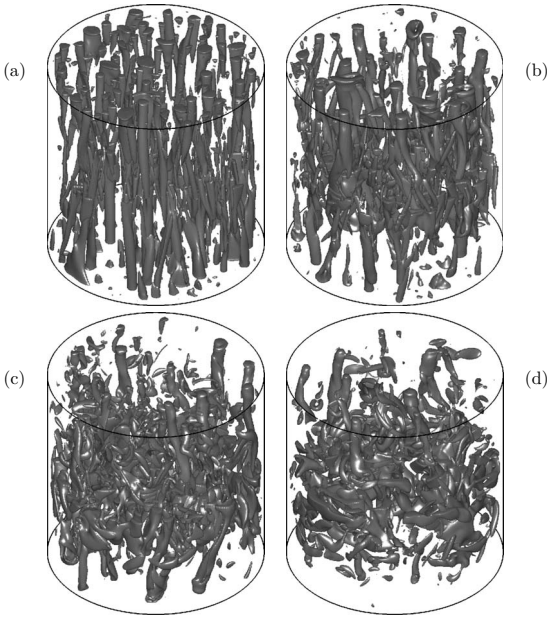


FIG. 4. Snapshots of $Q_{3D}$ isosurfaces at (a) $\mathrm{Ta}=1.9\times10^{10}$, (b) $\mathrm{Ta}=4.8\times10^{9}$, (c) $\mathrm{Ta}=1.2\times10^{9}$, and (d) $\mathrm{Ta}=3.0\times10^{8}$.

### C. Gathering of vortex statistics

The following analysis based on $Q$ has been carried out to quantify the vortex number density $N$, as well as the mean radius $r$ and circulation $\gamma$ per vortex. On a horizontal cylinder cross-section, contours of $Q_{3D}$ are drawn at a threshold value equal to the root-mean-square $Q_{3D,rms}$ for the simulations. For the experimental results we draw contours of $Q_{2D}$ at a value $Q_{2D,rms}$ on the entire rectangular measurement section. The enclosed area $A$ per contour is calculated. A lower bound for the vortex area $A_{min}/H^2=1\times10^{-4}$ is applied to eliminate small-scale fluctuations. This minimal area is based on the grid resolution of the SPIV results: $A_{min}\approx\Delta x\times\Delta y$. The vortices found in the flow are considerably larger than this minimal area; the smallest mean vortex area found in this work is about six times $A_{min}$. Separate statistics are calculated for cyclonic and anticyclonic vortices; the distinction is made based on the sign of the vertical component of vorticity at the center of the vortex. The number of vortices counted in the experimental results is corrected for the fact that only part of the full cylinder cross-section can be measured. $N_+$ and $N_-$ thus, respectively, represent the number of cyclonic and anticyclonic vortices found in one complete cylinder cross-section.

The mean vortex radius $r$ is based on the vortex area $A$ found previously and is calculated as $r=\sqrt{A/\pi}$. It thus represents the radius that would belong to a circular vortex of area $A$. The vortex radius is averaged over all vortices found in the cross-section; again, a distinction is made between cyclones ($r_+$) and anticyclones ($r_-$). It is also possible to calculate a mean circulation $\gamma$ for the detected vortices. The cross-sectional area of the vortex is assumed to be filled with a constant vertical-vorticity level equal to half the vertical vorticity at the center of the vortex,

$$\gamma_{\pm} \equiv \tfrac{1}{2} A \omega_{z,\mathrm{center}}, \tag{6}$$

in which we also discern between cyclonic ($\gamma_+$) and anticyclonic ($\gamma_-$) vortices.

These results per snapshot are averaged in time as follows. Five independent velocity snapshots per rotation rate are used from the numerical simulations; only minor variations of the vortex statistics were found between the snapshots. For the experiments one in every 50 velocity maps (one every 3.3 s) is treated with the aforementioned analysis, followed by averaging. This procedure has been repeated with a different starting frame to avoid any bias, and also using one every 100 velocity maps. The results are essentially identical in all cases.

As mentioned before the threshold of $Q$ is chosen to be the root-mean-square value. This value is determined separately for each rotation rate and for each measurement height. It was found that this threshold value is high enough to discount the turbulent fluctuations in $Q$. A lower threshold leads to increasingly distorted nonconvex contours, making it harder to justify the classification as columnar vortices. At a threshold of twice the rms value there are less vortices detected, with a smaller radius and weaker circulation (due to the reduced area). Since generally the anticyclones are weaker (which entails a lower $Q$ value), the anticyclone density is reduced more than the cyclone density. In practice our choice of the threshold value is found to be close to the optimal one; basically all convex contours belonging to vortices are detected.

### D. Vortex statistics at constant height

Two fixed measurement heights inside the cylinder are considered: $z=0.8H$ (experiments and simulations), and $z=0.95H$ (simulations only). In Fig. 5 the mean number of cyclonic/anticyclonic vortices $N_{\pm}$ are shown as a function of Ta. The results at height $z=0.8H$ in Figs. 5(a) and 5(c) show no strong dependence on Ta. A slight upward trend of increasing vortex density with growing Taylor number may be present, but given the error bars we cannot provide a definitive conclusion. There is a good agreement between the results from experiment and simulation. There is an approximate balance between cyclones and anticyclones. At height $z=0.95H$, Fig. 5(b), at the highest three Taylor numbers, there are considerably more vortices detected than at $z=0.8H$. Apparently, many (cyclonic) vortices formed near the top do not stretch far downward before dissolving as they are not observed anymore at $z=0.8H$. This conclusion is also evident in the visualizations in Fig. 3 and 4. The population of anticyclonic vortices at $z=0.8H$ is larger than at $z=0.95H$ for all Taylor numbers. The formation of cyclonic vortices is triggered by the viscous Ekman-like boundary layer. Anticyclonic vortices apparently cannot penetrate into this layer; they are dissolved just above (bottom plate) or below (top plate) the Ekman layer. For reference, the thickness of the viscous boundary layer (based on the peak rms velocity parallel to the wall [25]) was found to be $\delta_\nu = 0.020H$ at $\mathrm{Ta}=3.0\times10^8$, scaling roughly as $\delta_\nu \sim \mathrm{Ta}^{-1/4}$, i.e., the boundary layer is thinner at higher Ta. A sign of the reduced boundary layer thickness is the appearance of more

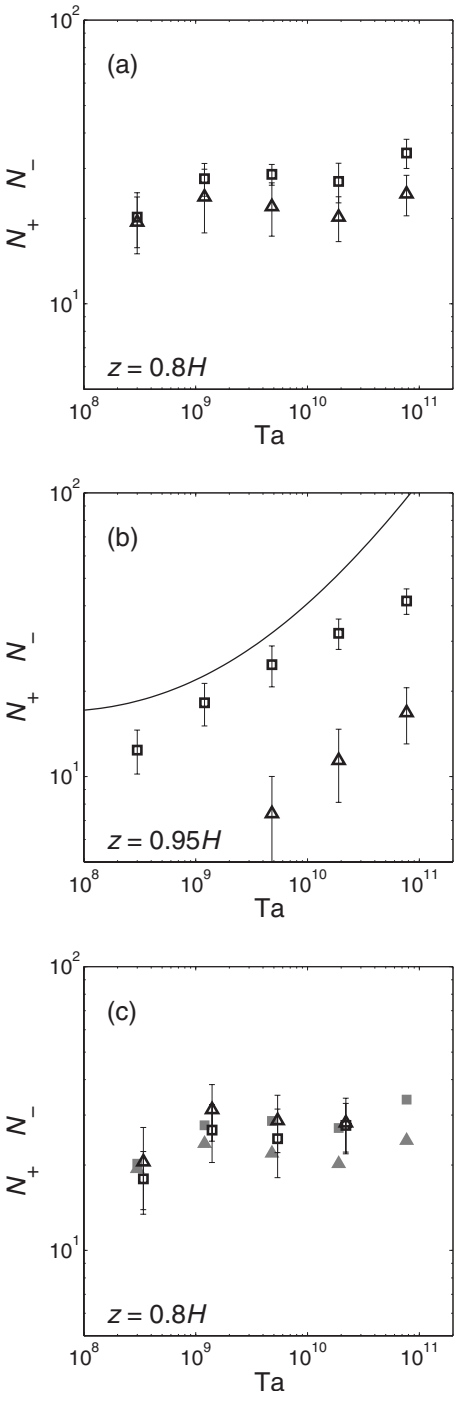


FIG. 5. Vortex number statistics from the simulations, at (a) $z=0.8H$ and (b) $z=0.95H$. Mean number of cyclones $N_+$ (squares) and anticyclones $N_-$ (triangles) are included. The solid line in (b) is Sakai's result for $N_+$ at the current parameter values [9]. (c) Mean vortex densities at $z=0.8H$ from the experiments (open black symbols). The simulation results from (a) are also included for reference (filled gray symbols).

anticyclonic vortices at height $z=0.95H$ for the cases $\mathrm{Ta} \geq 4.8\times10^9$. It must be noted that intermittently anticyclones are found also at the lowest Taylor numbers. In all cases their number is low; the intermittent nature prohibits averaging.

Vorobieff and Ecke [11] also investigated the characteristics of the vortical plumes. They reported vortex number densities linearly dependent on $\Omega$, which implies $N \sim \mathrm{Ta}^{1/2}$. Here, at $z=0.95H$, the height most comparable to the measurement position used by Vorobieff and Ecke, we obtain a flatter scaling for the cyclones which could be approximated by a scaling exponent $N_+ \sim \mathrm{Ta}^{0.2}$. Furthermore, the number of anticyclones in [11] is always considerably less than the number of cyclones; the first anticyclones are detected for $\mathrm{Ta}=1.4\times10^9$ (at $\mathrm{Ra}=3.2\times10^8$). Here a similar result is found, although the rotational dependence is weaker.

Boubnov and Golitsyn [8] reported an empirical relation $N_+ \sim \Omega \sim \mathrm{Ta}^{1/2}$ for unsteady air-cooled convection without a top plate, based on streakline photography. They did not report the occurrence of anticyclonic vortices. This may well be due to the difficulty of detecting anticyclones among the dominant cyclones using their measurement technique, along with the notion that the anticyclones do not reach the surface. In a study by Sakai [9] a model was derived for the horizontal separation between vortices, based on geostrophic dynamics, Ekman boundary layers and a heat flux correlation that is assumed independent of rotation. The model result is included in Fig. 5(b) with a solid line; the theory predicts $N_+$ as a function of Ra and Ta. The boundary layer thicknesses are estimated as $\delta_\mathrm{T}/H=3.8\mathrm{Ra}^{-1/3}$ for the thermal boundary layer and $\delta_\mathrm{E}/H=\mathrm{Ek}^{1/2}=\sqrt{2}\mathrm{Ta}^{-1/4}$ for the viscous Ekman layer. The thermal boundary layer thickness is based on the Nusselt number Nu as $\delta_\mathrm{T}/H=1/(2\mathrm{Nu})$, a formulation that is often used in non- rotating convection, completed with an experimentally obtained Nu-Ra correlation for the nonrotating case. Although the Nusselt number shows a considerable dependence on rotation [17,23], the thermal boundary layer thickness appears to be well approximated by this formulation for the current parameter range [25]. One limiting case of the theory, when $\delta_\mathrm{E} \gg \delta_\mathrm{T}$, is $N_+ \sim \mathrm{Ta}^{-1/4}$; the other limit, for $\delta_\mathrm{T} \gg \delta_\mathrm{E}$, is $N_+ \sim \mathrm{Ta}^{3/4}$. It was stated in [9] that this last limit does not apply when the critical rotation rate for suppression of convection [7] is approached, since then the heat flux is strongly reduced by rotation. At the current values we are quite far from either limit: $\delta_\mathrm{T}/H \approx 5\times10^{-3}$ and $3\times10^{-3} \lesssim \delta_\mathrm{E}/H \lesssim 1\times10^{-2}$. There is considerable disagreement between Sakai's prediction and the current results at both the lowest and the highest Taylor numbers under consideration. Both these Ta values may well be outside of the range of applicability of Sakai's theory. From the current results and the findings of the other studies, we can only conclude that the observed vortex number density scaling is strongly dependent on the method of vortex detection as well as the exact parameter range under consideration.

In Fig. 6 the mean vortex radii are presented. There is again only a very minor dependence on Ta. The average vortex radii are slowly decreasing with increasing Ta. Cyclones and anticyclones are of the same size. In Fig. 6(c) there is a notable difference between the results from the simulations (filled gray symbols) and the experiments (open black symbols). We expect that the discrepancy is primarily related with the non-perfect thermal conductivity of the top plate in the experiment.

We have tried a simple model for the top boundary in applying the Biot condition as boundary condition for temperature, i.e., the local plate temperature $T_p$ and the temperature gradient at the plate are (in dimensionless form) related as

$$T_p = -\frac{h}{H}\frac{\lambda_w}{\lambda_p}\left.\frac{\partial T}{\partial z}\right|_{z=H}, \tag{7}$$

where $h$ is the plate thickness, and $\lambda_p$ ($\lambda_w$) the thermal conductivity of Plexiglas (water). The numerical values of the parameters were chosen to match with the experiment: $h$

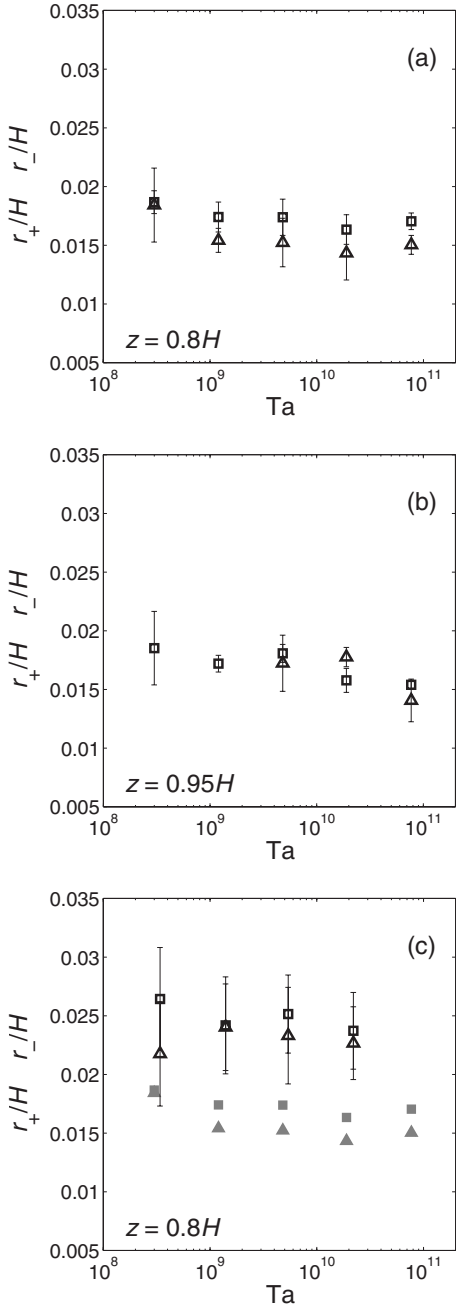


FIG. 6. Mean vortex radii from the simulations, at (a) $z=0.8H$ and (b) $z=0.95H$. Radii $r_+$ (squares) and $r_-$ (triangles) are included. (c) Mean vortex radii at $z=0.8H$ from the experiments (open black symbols). The simulation results from (a) are also included for reference (filled gray symbols).

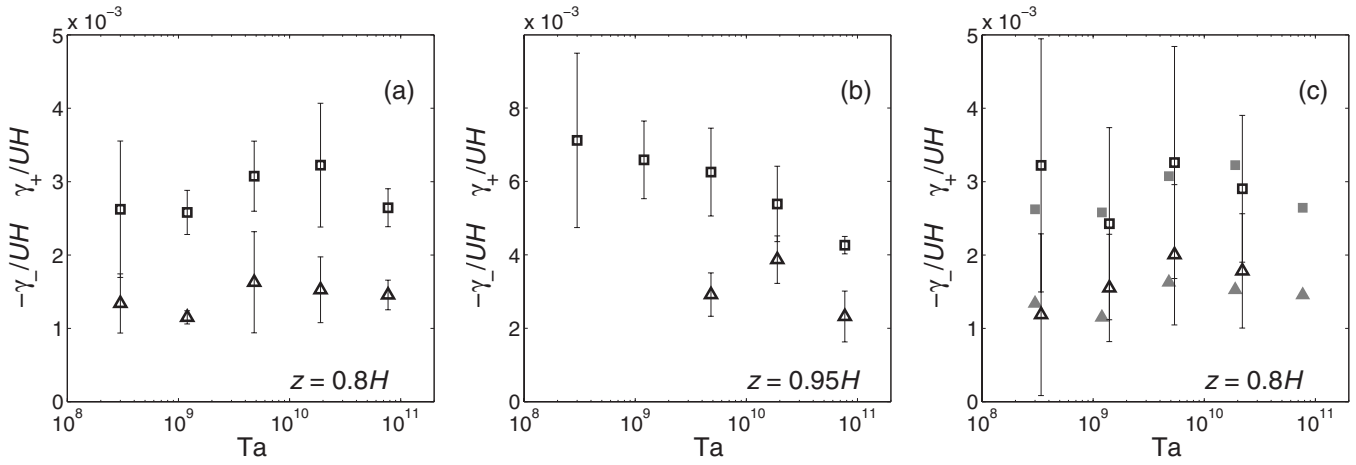


FIG. 7. Mean vortex circulation $\gamma_{\pm}$ as a function of Ta from the simulations, at (a) $z=0.8H$ and (b) $z=0.95H$. The mean circulation of cyclonic vortices $\gamma_+$ is depicted with squares; for anticyclones $-\gamma_-$ is shown with triangles (the minus sign is included since $\gamma_-<0$). (c) Mean vortex circulation at $z=0.8H$ from the experiments (open black symbols). The simulation results from (a) are also included for reference (filled gray symbols).

$=1$ mm, $H=230$ mm, $\lambda_p=0.19$ W m$^{-1}$ K$^{-1}$, and $\lambda_w=0.60$ W m$^{-1}$ K$^{-1}$. No significant changes in the statistics have been observed. An important issue that is missing from the Biot model is the delayed temporal response of the Plexiglas plate to changes in the temperature distribution. The approach proposed by Verzicco [35], to solve the heat conduction equation on a mesh inside the plate in addition to the fluid motion, is probably needed to reconcile the results. However, this is beyond the scope of the current paper.

Vorobieff and Ecke [15] also report vortex radii obtained from an experiment at Rayleigh number $\mathrm{Ra}=2\times10^8$. The vortex radii from [15] are generally larger than those reported here. Furthermore, the dependence on the rotation rate is stronger in their results than it is in the current work. We cannot explain the discrepancy between the two studies, although it is expected that the vortex detection method plays an important role.

The dependence of the vortex circulation on Ta is presented in Fig. 7. At $z=0.8H$ the circulation of the vortices is largely unaffected by rotation. At $z=0.95H$ a stronger dependence on Ta is found. At the lowest Ta values the cyclonic vortices are very strong, in the sense that their circulation value is high [compare the vertical scales of Figs. 7(a) and 7(c) to Fig. 7(b)]. As the Taylor number increases the cyclonic circulation decreases, while the anticyclonic vortices become stronger. The difference between the mean circulation of cyclones and anticyclones is smallest at the higher Ta values under consideration. Still, cyclones are preferred in number, i.e., there are more cyclones than anticyclones.

Comparing Figs. 7(a) and 7(b), a strong vertical decay of the circulation of the vortices is readily observed. At the lowest Ta value the cyclonic circulation decreases by a factor three between $z=0.95H$ and $z=0.8H$. Vorticity is injected near the plates into vortices with strong circulation, but the circulation is rapidly lost when the vortex moves vertically downward. At $\mathrm{Ta}=7.7\times10^{10}$, about 35% of cyclonic circulation is lost between the two heights. Anticyclonic circulation is roughly 40% lower at $z=0.8H$ than at $z=0.95H$. Given that the measured vortex radii at the two heights are more or less equal (see Fig. 7), the loss of circulation between $z=0.95H$ and $z=0.8H$ must be due to a reduction of vertical vorticity. The findings concerning the circulation match with the results of [15], who found a 50% decrease of the maximal (minimal) vertical-vorticity value within cyclonic (anticyclonic) vortices when comparing measurements near the top plate and at $z=0.75H$, respectively. In Fig. 7(c) there is again good agreement between experimental (black open symbols) and numerical (gray filled symbols) results, showing that at $z=0.8H$ the cyclonic vortices possess more circulation than their anticyclonic counterparts.

### E. Vortex statistics at Ekman length scales

The vortex statistics at constant height have provided the opportunity to compare the experimental and numerical results with each other and with results from previous studies. It is found that the Ekman layer thickness $\delta_E/H$ is an important length scale for the formation of cyclonic vortices and the dissipation of anticyclonic vortices near the bottom and top plates. Therefore we repeat the analysis of the simulation results at heights $\delta_E/H$, $2\delta_E/H$, $3\delta_E/H$, and $5\delta_E/H$ from the top plate, respectively. In each case the vertical grid points nearest to the value $z=1-n\delta_E/H$ ($n\in\{1,2,3,5\}$) are used; the correspondence between the height under consideration and the exact value $1-n\delta_E/H$ was always within 5%. The results of this $\delta_E$-dependent analysis are depicted in Fig. 8. We again consider vortex number density $N_{\pm}$, vortex radius $r_{\pm}$, and vortex circulation $\gamma_{\pm}$, determined separately for cyclonic and anticyclonic vortices.

A first conclusion from the vortex densities as shown in Fig. 8(a) is that hardly any anticyclones are detected. Anticyclones are only detected for distances from the plate of $2\delta_E/H$ or more. Anticyclones are dissipated quite far from the Ekman boundary layer; only at the highest Ta values they can approach the plate up to a distance between $\delta_E/H$ and $2\delta_E/H$. The cyclone densities $N_+$ determined at heights between $2\delta_E/H$ and $5\delta_E/H$ are essentially the same. At height $\delta_E/H$ less cyclones are found. The formation of the cyclones

thus takes place in a layer with a thickness of approximately $2\delta_E/H$, consistent with the viscous boundary layer thickness we reported before [25] based on the distance from the plate to the position where the rms azimuthal velocity is maximal. The cyclone densities found at height $2\delta_E/H$ also match with the results obtained at constant height $z=0.95H$ in Fig. 5(b).

The mean vortex radii of the cyclones in Fig. 8(b) do not vary much with Ta when compared per Ekman level. Only at the lowest Ta there is a rather large discrepancy, which may point at a different vortex structure and/or vortex formation process in that case. The influence of the Ekman layer is weakest in that case due to the relatively low rotation rate (in other words a rather large Ekman number). At the three intermediate Taylor numbers under consideration here it is observed that the vortices grow in size as the distance to the plate increases. At the highest Ta, for distances to the plate of $2\delta_E/H$ and higher the cyclones remain of equal size, which again is an indication of the dominant columnar flow structuring in geostrophic flow (Taylor-Proudman theorem). The anticyclonic vortices that are detected have a larger radius, which is indicative of their dissipation through the spin-down process that causes a radial expansion.

In Fig. 8(c) the vortex circulation is presented. At each Taylor number the maximal circulation is found at a height $2\delta_E/H$. This consolidates the view that the vortices are formed in the boundary layer of thickness $2\delta_E/H$. The columns gradually lose circulation while moving vertically through the bulk region. Again, at the lowest Ta a somewhat different behavior from the other Ta cases is observed. The circulation per vortex is much larger, but the vortices lose their circulation more rapidly as they move away from the top plate. Consider Fig. 7(a), where the circulation per vortex has about the same value for all Taylor number cases. The anticyclonic vortices contain about the same circulation magnitude as the cyclones at the highest Ta.

## IV. CONCLUSION

Characteristics on the size, number density, and circulation of the vortex population in turbulent rotating convection have been obtained. Generally, there are more cyclonic than anticyclonic vortices. At constant height $z=0.8H$ the vortex densities are about the same at each of the considered Taylor numbers. Closer to the top plate ($z=0.95H$) the vortex number density increases as Ta grows. The vortex radii are largely independent of rotation. Cyclonic vortices possess a greater circulation than their anticyclonic counterparts, although at height $z=0.95H$ the difference between the two diminishes for higher Ta. The vortex statistics are also gathered in terms of the Ekman length scale $\delta_E/H$. Cyclonic vortices are formed inside a viscous boundary layer of approximate thickness $2\delta_E/H$. Anticyclonic vortices are dissipated well outside of this layer at greater distances from the plate.

It is remarkable that overall the vortex number densities and radii are considerably less dependent on rotation (Taylor number) than results reported in the literature [8,9,11,15]. The greatest difference between these studies, and thus a possible cause of the discrepancy, lies with the employed vortex detection methods. In this work we introduced an automated method that avoids arbitrary detection by eye. Unfortunately, a reconciliation of the results of the various studies remains out of reach for now.

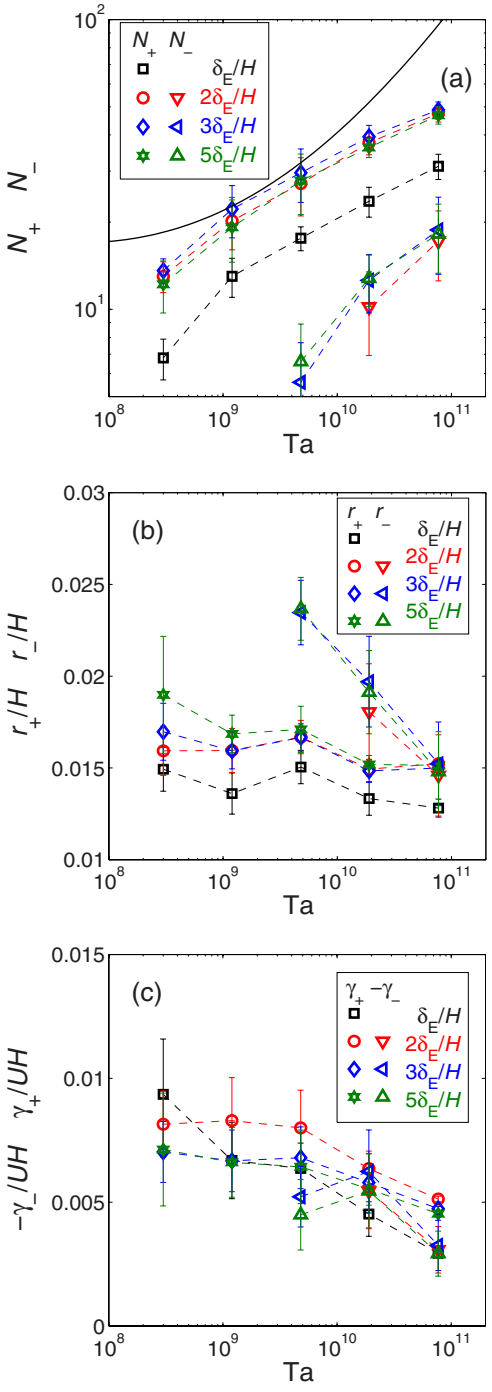


FIG. 8. (Color online) Vortex statistics from the simulations at vertical distances $\delta_E/H$ (squares for cyclones; black), $2\delta_E/H$ (circles for cyclones, down triangles for anticyclones; red online), $3\delta_E/H$ (diamonds for cyclones, left triangles for anticyclones; blue online), and $5\delta_E/H$ (stars for cyclones, up triangles for anticyclones; green online) from the top plate. (a) Vortex densities $N_+$ and $N_-$. The solid black line represents Sakai's model [9]. (b) Mean vortex radii $r_+$ and $r_-$. (c) Mean vortex circulations $\gamma_+$ and $-\gamma_-$. Dashed lines are guides for the eyes.

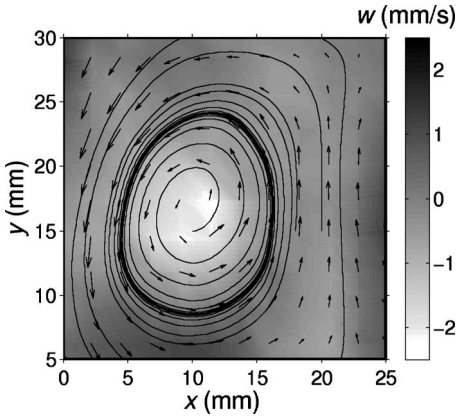


FIG. 9. Velocity snapshot of a vortex measured at $z=0.8H$, Ta $=2.2\times10^{10}$. Horizontal velocity is indicated with arrows, while the gray background coloring represents vertical velocity. Solid lines are instantaneous streamlines based on the horizontal velocity.

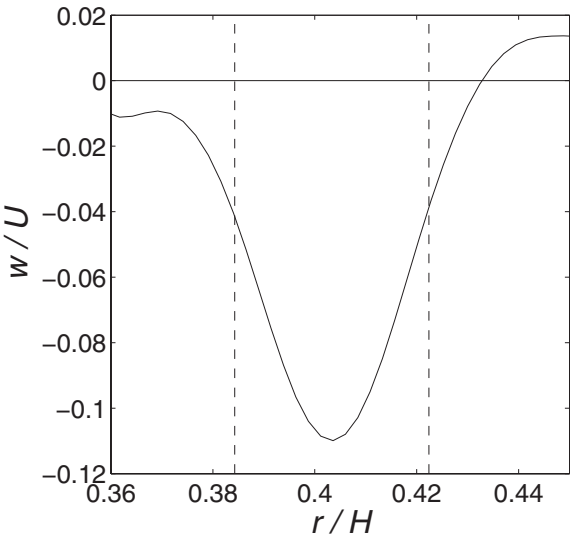


FIG. 11. Radial cross-sectional plot through a vortex of the vertical component of velocity $w$. The dashed lines indicate the radial positions of the limit cycle as observed in Fig. 10(b).


## ACKNOWLEDGMENTS

R.P.J.K. wishes to thank the Foundation for Fundamental Research on Matter (Stichting voor Fundamenteel Onderzoek der Materie, FOM) for financial support. This work was sponsored by the National Computing Facilities Foundation (NCF) for the use of supercomputer facilities, with financial support from the Netherlands Organization for Scientific Research (NWO).


## APPENDIX: VORTEX STRUCTURE FROM INSTANTANEOUS STREAMLINES

In the previous works by Vorobieff and Ecke [11,15] the PIV velocity fields were also investigated with instantaneous two-dimensional streamlines. Recording velocity fields very close to the top plate, it was argued that vertical velocities will be small. In this range the instantaneous streamline pattern gives a realistic view of the flow pattern including the out-of-plane motion, which occurs in regions where streamlines join. Vorobieff and Ecke saw a limit-cycle-like behavior of the streamlines around a cyclonic vortex: streamlines from within the vortex center would spiral outward toward a near-ellipsoidal trajectory around the vortex center, while streamlines from outside the limit cycle spiral inward toward it. These authors linked this streamline pattern around vortices near the top wall with a vertical-velocity structure of flow toward the plate in the vortex core and flow directed away from the plate in the limit-cycle region around the core. See Fig. 6 of [15] and Fig. 9 of [11].

We also investigated the velocity field measured with SPIV at $z=0.8H$ using instantaneous streamlines based on the horizontal components of velocity. A typical result is pre-

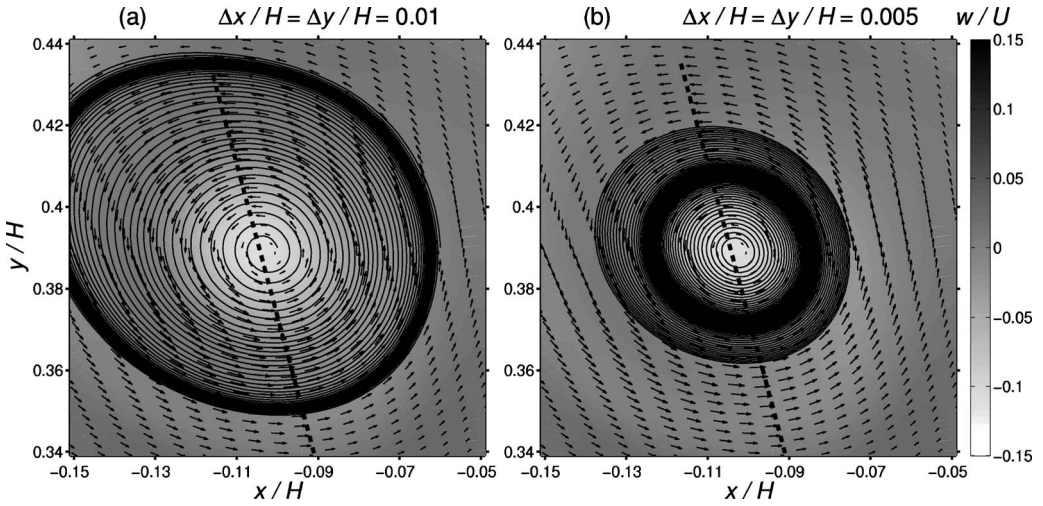


FIG. 10. Velocity snapshot of a vortex from a simulation, taken at $z=0.8H$ and Ta$=1.9\times10^{10}$. Horizontal velocity is indicated with arrows; the vertical component is depicted with the gray colored background. Solid lines are instantaneous streamlines calculated from interpolated horizontal-velocity fields on a Cartesian grid at two grid resolutions: (a) grid spacing $\Delta x=\Delta y=0.01H$; (b) grid spacing $\Delta x=\Delta y=0.005H$. The dashed line represents the line of intersection for the vertical-velocity plot in Fig. 11.

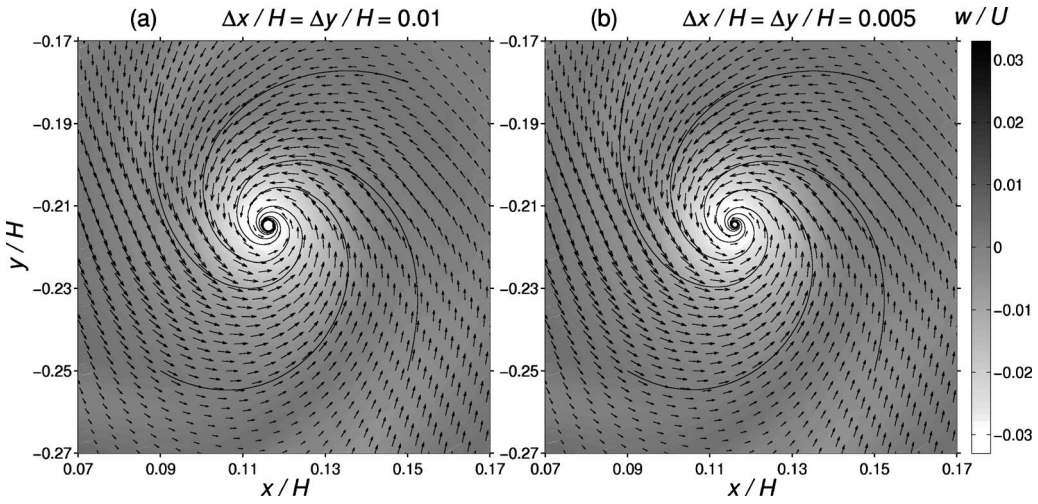


FIG. 12. Velocity snapshot of a vortex from a simulation, taken at $z=0.997H$ and $\mathrm{Ta}=1.9\times10^{10}$. Horizontal velocity is indicated with arrows; the vertical component is depicted with the gray colored background. Solid lines are instantaneous streamlines calculated from interpolated horizontal-velocity fields on a Cartesian grid at two grid resolutions: (a) grid spacing $\Delta x=\Delta y=0.01H$; (b) grid spacing $\Delta x=\Delta y=0.005H$.

sented in Fig. 9, which depicts the region around a vortex at $\mathrm{Ta}=2.2\times10^{10}$. The background coloring indicates the vertical velocity, while the arrows depict the horizontal parts. Instantaneous streamlines (solid black lines) indeed form a similar limit cycle around the vortex core. However, the limit cycle is not reproduced in the vertical velocity; from the reasoning presented above an upward motion is expected around the limit cycle.

This issue has been further addressed with the numerical simulations. The simulation results from this appendix stem from our calculations at $\mathrm{Ra}=1.0\times10^{9}$ [25]. A similar treatment of vortical regions using instantaneous streamlines has been carried out. A typical result is presented in Fig. 10 at height $z=0.8H$ and $\mathrm{Ta}=1.9\times10^{10}$. The velocity field on a grid in cylindrical coordinates is again shown using vectors and the background color. For the calculation of the streamlines these velocities were first interpolated to a Cartesian grid. In Fig. 10(a) the grid spacing of the interpolated field was $\Delta x=\Delta y=0.01H$, while in (b) it was $\Delta x=\Delta y=0.005H$. The resulting streamlines are not alike at all; they are dependent on the resolution. Compared with the experimental result (which has an even coarser resolution), the inward or outward spiraling is more gradually: only after many revolutions the streamlines reach the limit cycle. The vertical velocity again shows no distinct vertical-velocity signature in either of the limit cycles in Figs. 10(a) or 10(b). These points have been validated for other vortices as well. Thus we conclude that the limit-cycle behavior found in the instantaneous streamlines is no physical manifestation of the three-dimensional flow in the vortices. It is entirely caused by finite-resolution effects of the velocity field used in the calculation of the streamlines. Further evidence is provided in Fig. 11, where a cross-sectional profile of vertical velocity $w$ through the vortex is presented (the cross- section is along the dashed line in Fig. 10). The vertical velocity decreases and rises monotonically, with no sign of secondary vertical motions.

The measurement height is also important: especially very close to the bottom and top plates the streamlines based on two-dimensional horizontal velocity are expected to give reliable information on out-of-plane vertical motion. Therefore the analysis as before has been repeated for several vortices at heights $z=0.95H$ (not shown here) and $z=0.997H$ (Fig. 12). In the case $z=0.98H$ a similar picture arises as in Fig. 10, but with the limit cycle generally tighter around the vortex center. At $z=0.997H$, which is within the viscous boundary layer [25], the streamlines spiral inward as expected.

[1] H. L. Kuo, J. Atmos. Sci. **23**, 25 (1966).
[2] J. Marshall and F. Schott, Rev. Geophys. **37**, 1 (1999).
[3] F. H. Busse, Chaos **4**, 123 (1994).
[4] M. S. Miesch, Sol. Phys. **192**, 59 (2000).
[5] J.-C. Gascard, A. J. Watson, M.-J. Messias, K. A. Olsson, T. Johannessen, and K. Simonsen, Nature (London) **416**, 525 (2002).
[6] H. van Santen, C. R. Kleijn, and H. E. A. van den Akker, J. Cryst. Growth **212**, 299 (2000).
[7] S. Chandrasekhar, *Hydrodynamic and Hydromagnetic Stability* (Oxford University Press, Oxford, 1961).
[8] B. M. Boubnov and G. S. Golitsyn, J. Fluid Mech. **167**, 503 (1986).
[9] S. Sakai, J. Fluid Mech. **333**, 85 (1997).
[10] P. Vorobieff and R. E. Ecke, Phys. Fluids **10**, 2525 (1998).
[11] P. Vorobieff and R. E. Ecke, J. Fluid Mech. **458**, 191 (2002).
[12] H. J. S. Fernando, R.-R. Chen, and D. L. Boyer, J. Fluid Mech. **228**, 513 (1991).
[13] F. Zhong, R. E. Ecke, and V. Steinberg, J. Fluid Mech. **249**, 135 (1993).

[14] K. Julien, S. Legg, J. McWilliams, and J. Werne, J. Fluid Mech. **322**, 243 (1996).
[15] P. Vorobieff and R. E. Ecke, Physica D **123**, 153 (1998).
[16] M. Sprague, K. Julien, E. Knobloch, and J. Werne, J. Fluid Mech. **551**, 141 (2006).
[17] J.-Q. Zhong, R. J. A. M. Stevens, H. J. H. Clercx, R. Verzicco, D. Lohse, and G. Ahlers, Phys. Rev. Lett. **102**, 044502 (2009).
[18] M. Raffel, C. Willert, and J. Kompenhans, *Particle Image Velocimetry* (Springer, Berlin, 1998).
[19] J. W. Portegies, R. P. J. Kunnen, G. J. F. van Heijst, and J. Molenaar, Phys. Fluids **20**, 066602 (2008).
[20] J. C. R. Hunt, A. Wray, and P. Moin, Center for Turbulence Research Report No. CTR-S88, 1988 (unpublished).
[21] G. Haller, J. Fluid Mech. **525**, 1 (2005).
[22] R. P. J. Kunnen, H. J. H. Clercx, B. J. Geurts, L. J. A. van Bokhoven, R. A. D. Akkermans, and R. Verzicco, Phys. Rev. E **77**, 016302 (2008).
[23] R. P. J. Kunnen, H. J. H. Clercx, and B. J. Geurts, EPL **84**, 24001 (2008).
[24] R. P. J. Kunnen, H. J. H. Clercx, and B. J. Geurts, Phys. Rev. Lett. **101**, 174501 (2008).
[25] R. P. J. Kunnen, B. J. Geurts, and H. J. H. Clercx, J. Fluid Mech. **642**, 445 (2010).
[26] L. Prandtl, Beitr. Phys. Atmos. **19**, 188 (1932).
[27] R. Verzicco and R. Camussi, Phys. Fluids **9**, 1287 (1997).
[28] R. Verzicco and P. Orlandi, J. Comput. Phys. **123**, 402 (1996).
[29] R. Verzicco and R. Camussi, J. Fluid Mech. **477**, 19 (2003).
[30] L. J. A. van Bokhoven, Ph.D. thesis, Eindhoven University of Technology, 2007.
[31] A. Okubo, Deep-Sea Res. **17**, 445 (1970).
[32] M. S. Chong, A. E. Perry, and B. J. Cantwell, Phys. Fluids A **2**, 765 (1990).
[33] J. Weiss, Physica D **48**, 273 (1991).
[34] J. Jeong and F. Hussain, J. Fluid Mech. **285**, 69 (1995).
[35] R. Verzicco, Phys. Fluids **16**, 1965 (2004).